# EXTENSIONS TO DSD THEORY:
## ANALYSIS OF PBX 9502 RATE STICK DATA[*]

T. D. Aslam, J. B. Bdzil and L. G. Hill
Los Alamos National Laboratory, Los Alamos, New Mexico, 87545

Recent extensions to DSD theory and modeling argue that in addition to the total shock-front curvature, the intrinsic front propagation law can depend on other variables. Here we outline this recent work and present results of high-resolution numerical simulations of 2D detonation that verify the theory on some points, but disagree with it on others. We discuss how these results impact the analysis of PBX 9502 shock curvature data.

## I-INTRODUCTION

The benefits of using insensitive high explosives (IHE) like PBX 9502 (9502) have been well documented [1]. These desirable features come at a price. The reaction zone is longer for IHEs, thus making them more nonideal. In real world applications, this translates into significant performance problems, such as problems with detonation wave spreading. The speed of detonation propagation is affected over large regions. To be realistic, calculations of performance must include reaction zone effects.

As we will show, to capture these effects on propagation with direct numerical simulation (DNS) requires roughly 50 cells in the streamwise direction of the reaction zone to get an error of no more than 50 m/s for the detonation speed. Considering only the volume occupied by the reaction zone, $V_{rz}$, in a 3D DNS $V_{rz} = a \cdot \mathcal{L}^2 \cdot \eta_{rz}$, where $\mathcal{L} \approx 200$mm is the system dimension, $\eta_{rz} \approx 1$mm is the reaction-zone length and $a$ is an $O(1)$ geometry factor. For 50 cells in the reaction zone, this

estimate yields $O(10^{10})$ cells at any instant just in the reaction zone. A time of $\underline{10^{-4}\text{s}}$ is required for one cell update for a modern high-order algorithm running on a Silicon Graphics (SGI) R10K processor. With a time step of roughly $\Delta t = 4 \times 10^{-3} \mu$s, a physical time of 50 $\mu$s corresponds to $1.25 \times 10^4$ time steps. This corresponds to a single processor computation time of

$$T_{cpu3D} = (10^{-4}\text{s}) \cdot (10^{10}\text{cells}) \cdot (1.25 \times 10^4\text{steps}) \quad (1)$$
$$= 1.45 \times 10^5 \text{days} .$$

With perfect parallelization over 1000 cpus, this becomes $T_{||3D} = 145$days. Because this estimate includes only one aspect of an engineering simulation and we do not achieve perfect parallel performance, this is an underestimate.

In place of DNS, we have advanced using detonation shock dynamics (DSD), a strategy in which the effects of the reaction zone are captured by a subscale front model [2]. Then detonation propagation is described by an analytical expression for the normal detonation speed, $D_n$, that depends on only intrinsic front related variables such as shock curvature, $\kappa$, yielding $D_n(\kappa)$. Fine zoning to simulate the reaction zone effects is then not required. With this approach, grid converged solutions of detonation propagation can be ob-
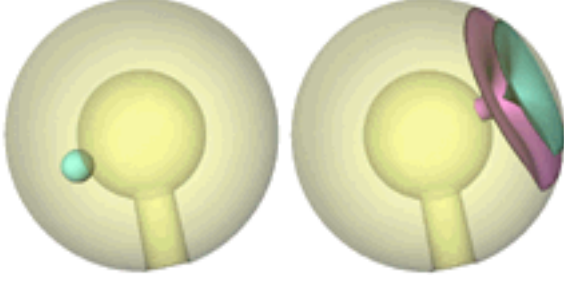
FIGURE 1. 3D HUYGENS AND DSD WAVE SPREADING CALCULATIONS FOR A 9502 SIMULANT. THE DSD WAVE IS SHOWN CLEARLY LAGGING HUYGENS. AN ALGORITHM BASED ON LEVEL-SET METHODS WAS USED.

tained in about an hour. Displayed in Fig. 1 is the results of such a calculation performed using level-set implementation of DSD [3]. The problem is 3D (due to the hole) and considers the "point" initiation of detonation in a shell of IHE. The offset between the two fronts at late time, shows the difference between Huygens and DSD for a 9502-like material.

In Sec. II of this paper, we briefly outline the derivation of an extended DSD front law that includes the effects of front acceleration, $DD_n/Dt$ and transverse flow, $\partial^2 D_n/\partial\xi^2$, where $\xi$ measures the arclength along the shock. This extends previous work of Yao & Stewart [4], Aslam & Stewart [5] and Short [6]. We explore the consequences that the modifications to $D_n(\kappa)$ bring. DSD is an asymptotic theory, based on perturbations about the reference state of an unsupported ZND detonation. To both verify the efficacy of the theory away from $D_{cj}$ and to more fully define the phase plane in which multi-D detonations live, we report the results of high-resolution DNS on the steady rate stick problem in Sec. III. This comparison indicates that, although the base $D_n(\kappa)$ gives a reasonable leading order description, for high-fidelity results the contributions of the extended theory are needed. Further, we find that when the phase velocity, $D_0$, differs between sticks by a small amount, the difference between $D_n$ vs $\kappa$ along the corresponding shocks is also small. Finally, in Sec. IV we carry all of our findings over to the analysis of 9502 curvature data, where the measured phase velocity differences are indeed small. We find that slightly different $D_n$ vs $\kappa$ forms are needed along different shocks. Because of the smallness of these differences, uncertainties in the data at high $\kappa$, no clear indication exists in the data on what direction the extensions should
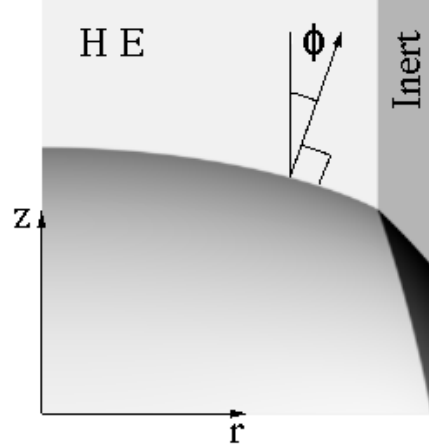


FIGURE 2. A GRAYSCALE RENDERING OF A 2D RATE STICK DNS. THE DETONATION TRAVELS UPWARDS, AND $r = 0$ MARKS THE PLANE OF SYMMETRY.

take. We argue that $D_n(\kappa)$ can provide a good average description.

## II-EXTENDED DSD THEORY

Consider the steady, detonation rate stick shown in Fig. 2. With a simple geometric argument, it is easily shown that the time rate of change in the shock normal direction, $D(\ )/Dt$ of $D_n$ is

$$\frac{DD_n}{Dt} = -(D_0 \sin \phi)^2 \kappa_s \ , \qquad (2)$$

where $D_0$ is the phase velocity, $\kappa_s$ is the slab component of the total curvature

$$\kappa \equiv \kappa_s + (\sin \phi)/r \ , \qquad (3)$$

with $\phi$ the shock angle and $r$ the local radius to a point on the shock. The basic tenants of DSD theory are: (1) the shock curvature is small measured on the scale of the 1D ZND reaction zone (i.e., $\kappa_s = O(\epsilon)$ with $\epsilon << 1$) and (2) the flow is quasisteady (i.e., time variations are slow). From Eq. (2) it then follows that where $\phi$ and $\sin \phi$ are order one (i.e., $O(1)$), then $DD_n/Dt = O(\kappa_s)$. Given the assumed slow time variations (say, with a scaled time, $\tilde{t} \equiv \epsilon t$), the departure of $D_n$ from $D_{cj}$ would need to be $O(1)$. Then the perturbations $\kappa_s$ and $DD_n/Dt$ would enter the theory at the same order, off of a base state that is far from CJ. This is the limit considered by Yao & Stewart [4].

Here we do something different. We adopt the "traditional" DSD scalings [2], where $\kappa_s = O(\epsilon)$, $\mathcal{D} = \epsilon\tilde{\mathcal{D}} = (D_n - D_{cj})/D_{cj}$ and

$$\phi = \epsilon^{1/2}\tilde{\phi} \,, \tilde{t} = \epsilon t \,, \tilde{\xi} = \epsilon^{1/2}\xi \,, \qquad (4)$$

where tilde'd variables are order one, $\xi$ is shock arclength and $\kappa_s = \epsilon\tilde{\phi}_{,\tilde{\xi}}$. Then $DD_n/Dt = O(\epsilon^2)$, and time dependence enters the theory at one order higher than does $\kappa_s$. Here we briefly outline the steps in the formal asymptotic analysis that leads to the higher-order propagation law

$$\bar{\kappa} = \mathcal{F}(\mathcal{D}) - A\frac{D\mathcal{D}}{Dt} + B\frac{\partial^2\mathcal{D}}{\partial\tilde{\xi}^2}, \qquad (5)$$

where the bared variables are dimensionless. We will study the properties of this law in some detail.

The basic physics that we study is described by the 2D Euler equations

$$\frac{\partial\rho}{\partial t} + \bar{\nabla}\cdot(\rho\bar{u}) = 0, \qquad (6)$$

$$\frac{\partial\rho\bar{u}}{\partial t} + \bar{\nabla}\cdot(\rho\bar{u}\bar{u} + \bar{\bar{I}}P) = 0, \qquad (7)$$

$$\frac{\partial\rho e}{\partial t} + \bar{\nabla}\cdot[(\rho e + P)\bar{u}] = 0, \qquad (8)$$

where $e = E + (\bar{u}\cdot\bar{u})/2$, $\rho$ is density, $\bar{u}$ is particle velocity, $P$ is pressure and the internal energy, $E(P,\rho,\lambda)$ is taken as the polytropic form

$$E(P,\rho,\lambda) = \frac{P/\rho}{\gamma - 1} - q\lambda, \qquad (9)$$

with $q$ the heat of detonation and $\lambda$ the reaction progress variable ($\lambda = 0$ is unreacted), which is governed by

$$\frac{d\lambda}{dt} \equiv R = k\sqrt{1 - \lambda}\left(\frac{P}{P_{cj}}\right)^n, \qquad (10)$$

where $k$ is the rate premultiplier and $n$ is an integer. We carry forward the analysis using the shock-based, intrinsic coordinates we've described and used before (*i.e.*, the Bertrand coordinates given in [2], [7]). The cartesian coordinates $(r, z)$ are replaced by shock arclength, $\xi$, and the distance along the local shock normal into the reaction zone, $\eta$. We further transform to $(\xi, \lambda)$ as independent variables (*i.e.*, $(r, z) \Rightarrow (\xi, \eta) \Rightarrow (\xi, \lambda)$). Written in these variables and expressed in quasi-conservative form, the 2D Euler equations become

$$[\rho(D_n - u_\eta)]_{,\lambda} = -\frac{\mathcal{A}}{(R - \mathcal{L}(\lambda))}, \quad (11)$$

$$\left[\rho(D_n - u_\eta)^2 + P\right]_{,\lambda} = \frac{\mathcal{B}}{(R - \mathcal{L}(\lambda))}, \quad (12)$$

$$\left[E + 1/2(D_n - u_\eta)^2 + \frac{P}{\rho}\right]_{,\lambda} = \frac{\mathcal{C}}{(R - \mathcal{L}(\lambda))}, \quad (13)$$

$$[u_\xi]_{,\lambda} = \frac{\mathcal{E}}{(R - \mathcal{L}(\lambda))}, \quad (14)$$

where

$$\mathcal{A} = (D_n - u_\eta)\cdot(\mathcal{G} + \mathcal{L}(\rho)), \qquad (15)$$

$$\begin{aligned}\mathcal{B} = (D_n - u_\eta)\cdot((u_\eta - D_n)\cdot\mathcal{G} + \rho\mathcal{H} \\ + \mathcal{L}(\rho(u_\eta - D_n)) + \rho\cdot\mathcal{L}(D_n)), \qquad (16)\end{aligned}$$

$$\begin{aligned}\mathcal{C} = (D_n - u_\eta)\cdot(\mathcal{H} + \mathcal{L}(D_n)) + \frac{1}{\rho}\mathcal{L}(P) \\ + -\mathcal{L}(E + 1/2(D_n - u_\eta)^2 + \frac{P}{\rho}), \qquad (17)\end{aligned}$$

$$\mathcal{E} = -\frac{P_{,\xi}}{\rho(1 - \eta\kappa_s)} + \frac{u_\eta}{u_\xi}\mathcal{H} - \mathcal{L}(u_\xi), \qquad (18)$$

$$\mathcal{G} = \frac{\rho}{(1 - \eta\kappa_s)}\left(\kappa_s u_\eta + u_{\xi,\xi}\right), \qquad (19)$$

$$\mathcal{H} = \frac{u_\xi}{(1 - \eta\kappa_s)}\left(D_{n,\xi} - \kappa_s u_\xi\right), \qquad (20)$$

and where through $O(\epsilon^2)$

$$\mathcal{L}(\ ) = \epsilon\frac{D}{D\tilde{t}} + \epsilon\frac{D\lambda^{(1)}}{D\tilde{t}}\frac{\partial}{\partial\lambda} + O(\epsilon^{2+\delta}), \qquad (21)$$

with $D(\ )/D\tilde{t}$ the scaled intrinsic, shock fixed time derivative (called the "dot" derivative, herein) and $\delta > 0$. Note, that we have used $,_x$ to indicate partial derivative with respect to $x$ in some places. To reiterate, Eqs. (11-14) are simply a rewrite of the complete, 2D, time-dependent Euler equations.

In forming the perturbation expansions of the dependent variables, we break with previous practice and take $\epsilon = \mathcal{D}/\tilde{\mathcal{D}}$ as the expansion or order parameter in place of $\kappa$ and expand

$$\kappa_s = \epsilon\kappa^{(1)} + \epsilon^2\kappa^{(2)} + \cdots. \qquad (22)$$

This is motivated by two things: (1) $\kappa_s(\mathcal{D})$ is single valued and (2) we anticipate this asymptotic expansion to have a larger range of validity. The remaining dependent variables are expanded as

$$\begin{aligned}Y = Y^{(0)} + \epsilon Y^{(1)} + \epsilon^2 Y^{(2)} + \cdots, \\ u_\xi = \epsilon^{3/2}u_\xi^{(3/2)} + \cdots, \qquad (23)\end{aligned}$$

where $Y = (\rho, u_\eta, P)^T$. We now trace the basic steps of the analysis.

At $O(1)$, the right hand sides of Eqs. (11-14) make no contribution (since they are $O(\epsilon)$) and we simply get the steady, unsupported ZND wave. Substituting the $O(1)$ solution into the right hand side of Eqs. (11-14), expanding the left hand side through $O(\epsilon)$ and integrating with respect to $\lambda$, yields at $O(\epsilon)$ the linear algebraic system

$$\bar{\bar{M}} \cdot \bar{Y}^{(1)} = \bar{N}^{(1)}, \tag{24}$$

where $\bar{\bar{M}}$ depends only on the $O(1)$ solution. Solving for $\bar{Y}^{(1)}$, we encounter a solvability condition arising from a singularity in $\bar{\bar{M}}^{-1}$ related to the sonic point of the base ZND problem. This condition returns the leading order eigenvalue relation similar to what we've presented before [8]

$$-\frac{D_{cj}\kappa^{(1)}}{k} = \left(\frac{\gamma+1}{\sqrt{2}\gamma}\right)^2 \left(\frac{h}{2^h - 1}\right) \tilde{\mathcal{D}} \equiv \frac{\tilde{\mathcal{D}}}{\alpha}, \tag{25}$$

where $h \equiv 3 - n$. The next term in the expansion is $O(\epsilon^{3/2})$, from which we obtain

$$u_{\xi,\lambda}^{(3/2)} = -\frac{1}{R^{(0)}\rho^{(0)}}P^{(1)}_{,\bar{\xi}} + \frac{D_{cj}u_\eta^{(0)}}{R^{(0)}}\tilde{\mathcal{D}}_{,\tilde{\xi}}, \tag{26}$$

which can be integrated to get $u_\xi^{(3/2)}$. The appearance of this term represents another point of departure from Yao & Stewart [4]; here transverse flow is included. Going on to $O(\epsilon^2)$, which completes the analysis presented here, yields

$$\bar{\bar{M}} \cdot \bar{Y}^{(2)} = \bar{N}^{(2)}. \tag{27}$$

With some help from *Maple* we can solve Eq. (27) and resolve the solvability condition to get

$$\kappa^{(2)}(\tilde{\mathcal{D}}^2, \frac{D\tilde{\mathcal{D}}}{D\tilde{t}}, \frac{\partial^2 \tilde{\mathcal{D}}}{\partial \tilde{\xi}^2}). \tag{28}$$

On combining this with $\kappa^{(1)}$, compressing the $\epsilon$ dependence and introducing the dimensionless variables

$$\bar{\kappa} \equiv \frac{\kappa_s D_{cj}}{k}, \bar{t} \equiv kt, \bar{\xi} \equiv \frac{k}{D_{cj}}\xi, \tag{29}$$

yields the extended intrinsic propagation law

$$\bar{\kappa} = \mathcal{F}(\mathcal{D}) - A\frac{D\mathcal{D}}{D\bar{t}} + B\frac{\partial^2 \mathcal{D}}{\partial \bar{\xi}^2} \tag{30}$$

where

$$\mathcal{F}(\mathcal{D}) = \frac{1}{\alpha}(-\mathcal{D} + \tilde{f}_2 \mathcal{D}^2), \tag{31}$$

and the coefficients $\tilde{f}_2$, $A$ and $B$ depend on $\gamma$ and $n$ in a complex way.

Equation (30) is a rigorously derived result for the limit of weak curvature and small departure of $D_n$ from $D_{cj}$. To try and extend the range over which this asymptotic expansion is valid, we appeal to the shock-change equation [9], which in our scaled variables is

$$\bar{\kappa} = -\frac{3(\gamma+1)}{2\gamma}(1+\mathcal{D})^{-2}\frac{D\mathcal{D}}{D\bar{t}} + \frac{3(\gamma+1)^2}{4\gamma(\gamma-1)}(1+\mathcal{D})^{-3}$$
$$\cdot \bar{R}\left(\frac{1}{6} + \frac{(\gamma+1)}{3}(1+\mathcal{D})^2 \left(\frac{\partial \bar{u}_\eta}{\partial \lambda}\right)_{\lambda=0}\right), \tag{32}$$

where $\bar{u}_\eta = u_\eta/D_n$ and $\bar{R} \equiv 2^n(1+\mathcal{D})^n$ is the scaled reaction rate along the shock. Equation (32) is exact along the detonation shock, although it is incomplete and needs closure with an independently supplied expression for $(\partial \bar{u}_\eta/\partial \lambda)_{\lambda=0}$. Its appeal lies with the strong nonlinear dependence (dynamic range) that it exhibits in its dependence on $\mathcal{D}$, something that our perturbation expansions lack. Our strategy is to develop an expression for $(\partial \bar{u}_\eta/\partial \lambda)_{\lambda=0}$ by expanding $u_\eta$ according to Eq. (23) and all other shock specific variables and derivatives as we have just described. Then matching term-by-term in powers of $\epsilon$ with Eq. (30) (with the $\epsilon$ dependence reinstated), a power series is developed for $(\partial \bar{u}_\eta/\partial \lambda)_{\lambda=0}$. With this series at hand, we note that it depends linearly on $(D\mathcal{D}/D\bar{t})$ and $(\partial^2\mathcal{D}/\partial\bar{\xi}^2)$ and suggests a simple (although nonlinear) dependence on $\mathcal{D}$. Appearing in this expression are series in $\mathcal{D}$ that beg summation

$$1 - 2\mathcal{D} + 3\mathcal{D}^2 + \cdots = (1+\mathcal{D})^{-2},$$
$$-\mathcal{D} - m\mathcal{D}^2 + \cdots = -\mathcal{D}(1+\mathcal{D})^m, \tag{33}$$

yielding forms that are extensible beyond $\mathcal{D} = O(\epsilon)$, where $m \equiv 1 - 2n - \tilde{f}_2$. With these associations made, we have as our approximation

$$\left(\frac{\partial \bar{u}_\eta}{\partial \lambda}\right)_{\lambda=0} = -\frac{(1+\mathcal{D})^{-2}}{2(\gamma+1)} - \frac{4\gamma(\gamma-1)}{2^n(\gamma+1)^3} \tag{34}$$
$$\cdot \left(\frac{\mathcal{D}(1+\mathcal{D})^m}{\alpha} + \left(A - \frac{3(\gamma+1)}{2\gamma}\right)\frac{D\mathcal{D}}{D\bar{t}} - B\frac{\partial^2 \mathcal{D}}{\partial \bar{\xi}^2}\right).$$

This expression limits properly as $\mathcal{D} \to 0$ and, as we shall see, provides a good asymptotic representation of the solution for $D_n/D_{cj}$ away from one. Clearly, there is some arbitrariness in the way we've reduced Eqs. (33) to closed form expressions.

Substituting Eq. (34) into Eq. (32), yields the detonation propagation law we now examine

$$(1+\mathcal{D})^{1-2n}\bar{\kappa} = -\frac{\mathcal{D}(1+\mathcal{D})^{1-2n-\tilde{f}_2}}{\alpha} + B\frac{\partial^2 \mathcal{D}}{\partial \bar{\xi}^2}$$
$$-\left(A + \frac{3(\gamma+1)}{2\gamma}\left((1+\mathcal{D})^{-1-2n} - 1\right)\right)\frac{D\mathcal{D}}{D\bar{t}}. \quad (35)$$

Equation (35) leads to a parabolic equation for the evolution of the front, which has a number of benefits. Next we examine the properties attendant to this front dynamics for some special cases. By systematically demagnifying the scales on which we view the solution (by making first the length and then the time scales longer, *i.e.*, $\epsilon\bar{\xi}$ and $\epsilon^2\bar{t}$), we can selectively drop the dependence of the solution on $(\partial^2\mathcal{D}/\partial\bar{\xi}^2)$ and then further its dependence on $(D\mathcal{D}/D\bar{t})$. We define a shorthand with which to describe these various limits: (1) Dnxixi denotes the complete model, (2) Dndot for the model with $(\partial^2\mathcal{D}/\partial\bar{\xi}^2)$ absent and (3) DnK for the model where $\bar{\kappa}$ depends only on $\mathcal{D}$. Next we examine the properties attendant to this front dynamics by considering some special cases.

The example we consider mimics 9502: $q = 4mm^2/\mu s^2$, $\gamma = 3$, $D_{cj} = 8.0mm/\mu s$ and $\rho_0 = 2gm/cc$. The parameters for Eq. (35) take the following values for this example: Case (1) $\underline{n=0}$, $k = 2.5147\mu s^{-1}$, $\tilde{f}_2 = 2.6581$, $A = 3.821$, $B = 0.2148$ and Case (2) $\underline{n=2}$, $k = 1.2936\mu s^{-1}$, $\tilde{f}_2 = -1.3636$, $A = 1.3319$, $B = 0.2024$. The rate premultiplier, $k$ has been adjusted so that the 1D ZND reaction-zone length is nearly $4\ mm$ for both cases. We now ask, for a sequence of steady rate sticks: (1) what are the structural differences between the models and (2) what are the differences in the predicted functions $D_n$ vs $\bar{\kappa}$ along the shocks for these models? We consider unconfined charges, which require that the sonic angle boundary condition be applied at the edge; $\phi_e = \arctan\sqrt{(\gamma-1)/(\gamma+1)} = 35.3^o$, for this equation of state example.

Structurally, the DnK and Dnxixi limits lead to parabolic evolution for the fronts and always predict smooth shocks. Any value of $\phi_e$ can be applied as an edge boundary condition. The Dndot
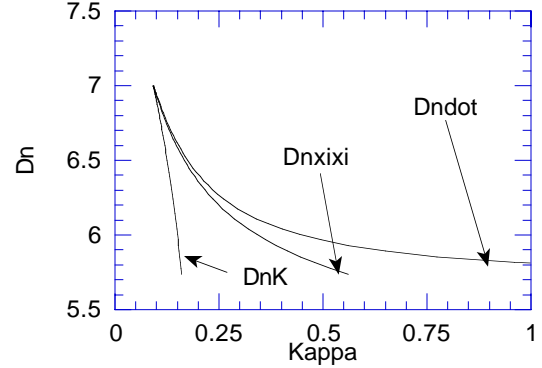


FIGURE 3. FOR CASE $n = 2$, A COMPARISON OF $D_n$ vs $\bar{\kappa}$ ALONG A $D_0 = 7.0\ mm/\mu s$ SHOCK. RESULTS FROM ALL THREE MODELS ARE SHOWN.

model generally leads to hyperbolic front dynamics and so can admit discontinuities in $\phi$ along the shock. However, the Dndot model has an upper limit for $\phi_e$, $(\phi_e)_{max}$. For the $n = 0$ case, $(\phi_e)_{max} = 28.5^o$.

We compare how the models differ in their predictions of the shocks. To do this, we compare the computed $D_n$ vs $\bar{\kappa}$ along the shocks as predicted by the DnK, Dndot and Dnxixi models. These results are shown in Fig. (3). The significant observation here is how much the higher-order models deviate from DnK and how relatively close they are to one another. Finally, we examine how small changes in the phase velocity effect $D_n$ vs $\bar{\kappa}$ along the corresponding shocks. We consider only the Dnxixi model and case $n = 2$, since it more nearly mimics 9502. Figure 4 shows that in the range of phase velocities observed for 9502, the differences in $D_n$ vs $\bar{\kappa}$ along the shocks is not large. If this behavior is obtained for the physical data for 9502, it will be hard to distinguish between the various modeling forms. We consider this issue in Sec. IV. Next we go on to describe the numerical simulations, the results they yield and compare these results with those for the models we have just described.

## III-DIRECT NUMERICAL SIMULATIONS

Direct numerical simulations were carried out for unconfined rate sticks for the model described in Sec. II. Since the simulations were to be used to both validate the theory and to expose new phenomena, we required the simulations to be very
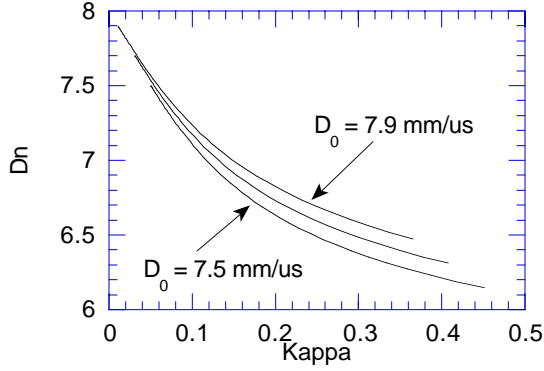
FIGURE 4. FOR CASE $n = 2$, A COMPARISON (USING THE Dnxixi MODEL) OF $D_n$ VS $\bar{\kappa}$ ALONG $D_0 = 7.5, 7.7, 7.9 \ mm/\mu s$ PHASE VELOCITY SHOCKS. THE SMALL DIFFERENCES ARGUE THAT WHEN THE PHASE VELOCITY DIFFERENCES ARE SMALL, IT WOULD BE DIFFICULT TO DISTINGUISH BETWEEN THE VARIOUS MODELS.

accurate. To get sufficient resolution of the reaction zone, the computational mesh was localized to the immediate vicinity of the reaction zone. Previously we had experienced problems with accuracy using standard shock capturing and interface algorithms. The shocks were either excessively thick (though smooth) for low order methods or noisy for higher-order methods. These artifacts produced $O(1)$ solution errors in things we care about, such as an increase in the reaction-zone length and problems with reaction ignition. Consequently, existing algorithms were modified and new ones developed [10] so as to enhance our ability to get higher-fidelity, grid converged solutions. A code was built around these algorithms for doing the rate stick problem.

The interior algorithm was based on the Lax-Friedrichs scheme, principally because it doesn't suffer from stability problem when computing waves that are stationary on the grid, such as is the case here [11]. A variant of the essentially nonoscillatory (ENO) algorithm of Osher, et al. [12] was used. To get high order spatial accuracy in smooth regions of the flow and smooth profiles near shocks, the high order spatial interpolation of the flux functions was obtained by using a convex combination of small stencil, local interpolants [13]. This has the property of smoothly transitioning to a monotone low order algorithm near shock waves. The shocks were still narrow, with 90% of the shock rise occurring monotonically in about 2 cells. A third order Runge Kutta
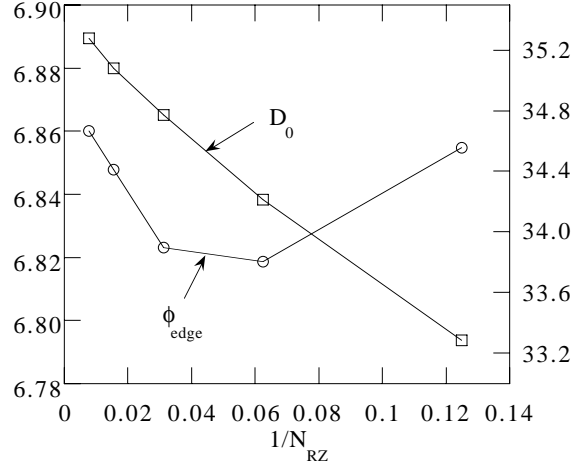


FIGURE 5. FOR CASE $n = 0$, A GRID CONVERGENCE STUDY FOR THE COMPUTED VALUE OF $\phi_e$ AND THE PHASE VELOCITY, $D_0$, FOR A 48 mm "RADIUS" 2D HE CHARGE. GOOD CONVERGENCE IS OBTAINED FOR $\phi_e$ TO THE EXACT VALUE OF $35°$. ABOUT 50 GRID POINTS ARE NEEDED IN THE REACTION ZONE TO GET $D_0$ GOOD TO $O(50 \ m/s)$.

method was used for the time integration.

A new interface algorithm (called the Ghost Fluid Method [10]) was developed that tracks the HE/confinement interface. It works by extending the calculation of fluid A across the interface into the region of fluid B (the virtual fluid is called the ghost fluid). This is done under the constraint of continuous pressure and normal particle velocity at the interface. This method goes a long way to eliminating the smearing and overheating artifacts found at captured and volume of fluid reconstructed interfaces. It allows for slip at the material interface, should that be desired. The location of the interface is then tracked with a level-set method based on solving an extended advection equation. Under resolution, the method is conserving of mass for stable interfaces.

To keep the calculation on a restricted spatial domain, mesh was recycled from regions downstream of the reaction zone that no longer influenced the reaction zone to upstream of the detonation shock. The time at which the detonation crossed a given laboratory $(z, r)$ point was recorded and saved as the array of values $(t, z, r)$, called the burn time table

$$t_b(z, r). \qquad (36)$$

By appropriately differentiating (differencing) these data, front intrinsic quantities such as $D_n$
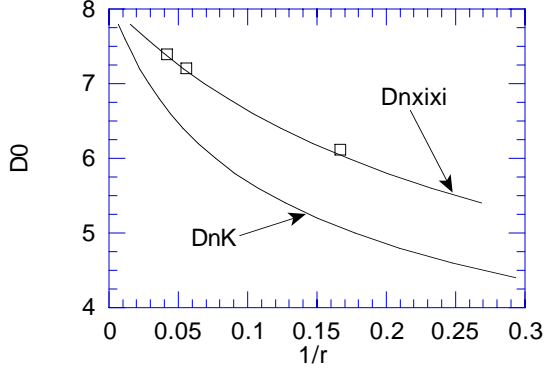
FIGURE 6. FOR CASE $n = 0$, SHOWN ARE THE DIAMETER EFFECT CURVES FOR THE Dnxixi and DnK MODELS AND RESULTS FROM HIGH-RESOLUTION DNS.
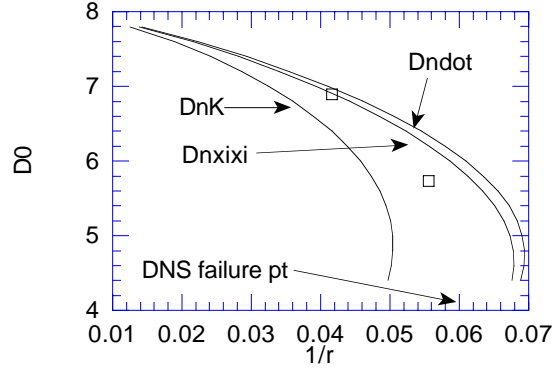


FIGURE 7. FOR CASE $n = 2$, SHOWN ARE THE DIAMETER EFFECT CURVES FOR THE Dnxixi, Dndot and DnK MODELS AND RESULTS FROM HIGH-RESOLUTION DNS.

and $\kappa_s$ could be calculated

$$\bar{n} = \frac{\bar{\nabla}(t_b)}{|\bar{\nabla}(t_b)|}, D_n = \frac{1}{|\bar{\nabla}(t_b)|}, \kappa_s = \bar{\nabla} \cdot \bar{n}, \quad (37)$$

where $\vec{n}$ is the unit vector in the shock normal direction.

If no special care is taken in differencing $t_b(z, r)$, quantities like $D_n$ can possess $O(1)$ errors and higher derivatives would diverge under grid refinement. By taking a stencil for the differencing that is greater than the minimum required, yet not so broad that spatial resolution is completely lost, grid converged values were obtained along most of the shock. Simple centered differences were used to compute the quantities in Eq. (37). The stencil width, $w$ was related to the order of the derivative, $m$ being computed and the grid spacing, $\Delta x$ by the expression

$$w \propto (\Delta x)^{\frac{1+m}{2+m}}. \quad (38)$$

Due to the $w$-step skipping of grid points, some of the higher derivatives could not be calculated within a few points of the HE charge boundary.

All of the calculations on which we report were run in parallel over 7-cpus of an 8-cpu, SGI-Origin. By way of example, we show how well all this numerical technology works by examining the convergence of the computed shock edge angle, $\phi_e$, a quantity for which we have the exact theoretical result of $\phi_e = 35.3^o$ for the equation of state of this problem. Figure 5 shows that under refinement, the computed $\phi_e$ is within $0.3^o$ of the exact value (the number of grid points in the reaction zone was 8, 16, 32, 64 and 128). Also shown is

the computed phase velocity (in $mm/\mu s$), where the errors are $O(50 \ m/s)$ even with 50 grid points in the reaction zone. These are the results for a simple easy to resolve problem. The situation is not nearly so "favorable" for more complex rate laws and problems.

Next we examine the predictions of the theoretically derived propagation laws against the numerical simulation results. Most of the results we show are from results having 128 points in the reaction zone. Displayed in Figs. (6-7) are the theoretically derived and DNS results (denoted as squares, □) for the diameter effect for cases $n = 0$ and $n = 2$, respectively. The three limits (Dnxixi, Dndot and DnK) are shown, with the exception that for case $n = 0$ Dndot isn't shown since it can not be made to satisfy the required edge angle boundary condition. Case $n = 2$ shows detonation failure (no steady solutions are found for $r$ less than some critical size), where case $n = 0$ does not. All the theoretical models follow this trend. The DnK model is clearly inferior to the other two, with the Dnxixi model having the best comparison overall.

Displayed in Fig. (8) is $D_n$ vs $\bar{\kappa}$ along the shock for the case $n = 2$. This example goes further to point out deficiencies in the DnK model. The more stringent comparison that the $D_n$ vs $\bar{\kappa}$ plane provides argues that the Dnxixi model provides the best overall agreement, tracking the DNS quite well. The Dnxixi model shows even better agreement for the case $n = 0$. The flatness of the Dndot model for large $\bar{\kappa}$ is evidence of the singularity in $\bar{\kappa}$ that occurs for $\phi$ just somewhat larger than $\phi_e$.
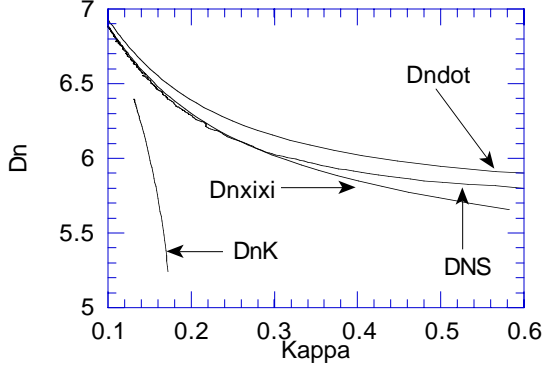
In the next section, we go on to consider how

FIGURE 8. FOR CASE $n = 2$, SHOWN IS A COMPARISON OF $D_n$ vs $\bar{\kappa}$ ALONG A 24 mm SHOCK FOR THE DNS, Dnxixi, Dndot AND DnK MODELS.

the ideas we have explored in Sec. II-III can be used to help analyze the physical data sets for 9502 collected by Davis, et al. [14].

## IV-ANALYSIS OF PBX 9502

The curvature measurements performed by Davis, et al. [14] were designed to yield high-quality data for the purpose of calibrating a $D_n(\kappa)$-law for 9502. Special care was taken so as to collect reliable data to the very edge of the charge. This was accomplished by affixing a mirrored glass plate (containing its own centering mark and spatial scales) to the front face of the charge as shown in Fig. (9). To have the physics of the wave arrival measurement be relatively unambiguous, the front face of the charge was machined at an oblique angle. Thus, oblique shock-driven mirror turning was responsible for deflecting the light from the optical axis of the camera. Since the mirror extended beyond the edge of the charge, a clean record was obtained to the very edge of the charge. Measurements were made for 10, 12, 18 and 50 mm diameter cylindrical sticks. This wave-front shape plus the phase velocity data was analyzed by postulating the existence of a unique $D_n(\kappa)$ function, of the form

$$\mathcal{D} = C_1 \cdot ((\kappa_c - \kappa)^\mu - \kappa_c^\mu) - \frac{C_2 \kappa^\nu}{1 + C_3 \kappa^\omega}, \quad (39)$$

where the parameters $C_1$, $C_2$, $C_3$, $\kappa_c$, $\nu$ and $\omega$ were constrained to be positive while $0 < \mu \leq 1$. The ansatz was that a single $D_n(\kappa)$ could be made to simultaneously fit all the data (phase velocities and shocks) and that $\phi_e$ and $D_{cj}$ were parameters (same for all the shocks) also to be determined in
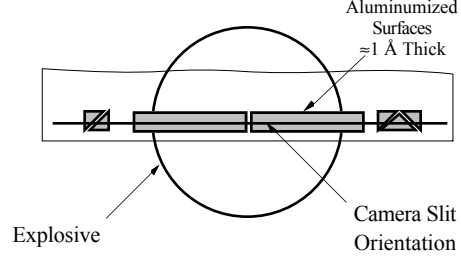


FIGURE 9. THE ANALYZING MIRRORED SURFACE USED IN THE 9502 CURVATURE MEASUREMENTS. THE EDGES OF THE MIRROR SERVED TO DEFINE THE SPATIAL SCALE.

the process. Under these assumptions, Eq. (39) could be integrated to get both a diameter-effect curve and the family of shock shapes. These numerically generated solutions were then systematically fit to the above described experimental data set using a Levenberg-Marquardt, nonlinear least squares algorithm.

The shocks (and corresponding phase velocities) were fit both individually and as part of a composite data set. When fit individually, the ($z$ vs $r$) shock data was fit with a total error of 0.5%, that was randomly distributed, and to within 10 $m/s$ for the phase velocities. For the composite data set, the shock error increased to 4%, with systematic variations localized near the charge boundary. The $D_n(\kappa)$ function obtained in this way are shown in Fig. (10). Considering the uncertainties in the data near the charge edge, the composite $D_n(\kappa)$ appears as a good representation of the data. Note that the trend towards $D_n$ vs $\bar{\kappa}$ curves of larger radius charges lying above those of smaller ones, shown in Fig. (4) by the Dnxixi model, is seen in the data. However, not shown is the trend of smaller charges going out to larger curvatures. In this instance, suspicion should be directed at the large curvature data obtained within a few percent of the charge boundary.

Based on the arguments presented in Sec. II and on the observation that the phase velocities differ by only 250 m/s, we expect that these data can not alone be used to select between the extended modeling forms we have discussed. Nevertheless, the increase in error of fit for the shocks from 0.5% to 4% suggests that improvements could be made over $D_n(\kappa)$. Given the good comparison of the newer Dnxixi model (and related Dndot model) with the DNS, we tried using the above described fitting algorithm with a Dndot form as the propagation model. We found
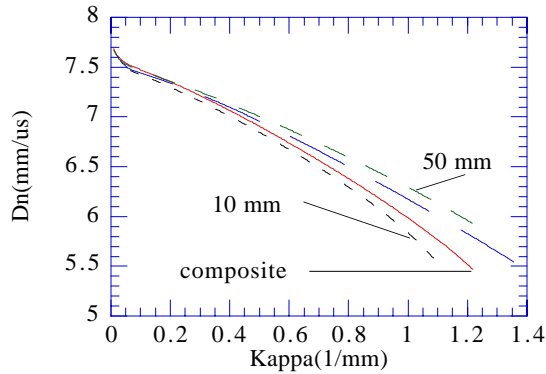
FIGURE 10. $D_n(\kappa)$ FOR PBX 9502 @ 25C. SHOWN ARE THE INDIVIDUAL FITS TO THE 10, 18 AND 50 mm SHOCKS ALONG WITH A COMPOSITE FIT TO ALL THE DATA. THE ARROWS INDICATE AT WHAT POINT WE ARE WITHIN 1% OF THE CHARGE BOUNDARY, BEYOND WHICH THE FITS ARE NOT SIGNIFICANT. THE PARAMETERS FOR THE COMPOSITE FIT ARE: $D_{cj} = 7.818 \ mm/\mu s$, $C_1 = 0.2643$, $\kappa_c = 1.276 \ mm^{-1}$, $\mu = 0.8042$, $C_2 = 0.1950$, $\nu = 0.5264$, $C_3 = 27.81$, $\omega = 1.279$ AND $\phi_e = 43^o$.

that the fit residuals were not improved over those obtained when using the DnK form. Given that the current data access only a small part of the phase space available to detonation propagation (with phase velocities differing by only 250 m/s), perhaps the addition of other data types could be used to better defining experimentally the parameters in higher-order models. As has been suggested, from a partial-differential equations point of view, the function $A(\mathcal{D})$ can be interpreted as the inverse of the square of the sound speed along the shock. Given this interpretation, equation of state data could then be used to independently constrain $A(\mathcal{D})$. However, the theoretical models we have developed, the DNS and the 9502 data we have analyzed all show that $A(\mathcal{D})$ decreases as $D_n$ increases. The sound speed does not have this property.

What does this argue? Perhaps that the data is not sufficiently accurate to differentiate between various extended models. To build these higher-order effects into the propagation law in a way that is inconsistent with the results from DNS and theory would be an error. Thus, given the current state of understanding, we do not propose a high-order intrinsic propagation law for PBX 9502 at this time. Experiments are needed that probe parts of the phase plane for multi-dimensional detonations that are not accessible

with rate sticks. We are currently examining "rib" data and nonsteady experiments, such as detonation corner turning.

## REFERENCES

[1.] B. Dobratz. LLNL explosives handbook: Properties of chemical explosives and explosive simulants. Technical Report UCRL-52997, Lawrence Livermore National Laboratory, 1981.

[2.] J. B. Bdzil and D. S. Stewart. *Phys. Fluids A*, 1:1261, 1989.

[3.] T. D. Aslam, J. B. Bdzil, and D. S. Stewart. *J. Comput. Phys.*, 126:390, 1996.

[4.] Jin Yao, , and D. S. Stewart. *J. Fluid Mech.*, 309:225, 1996.

[5.] T. D. Aslam and D. S. Stewart. *Combst. Theory Modelling*, 3:77, 1999.

[6.] Mark Short. *Combst. Theory Modelling*, 1:313, 1997.

[7.] J. B. Bdzil, W. Fickett, and D. S. Stewart. Detonation shock dynamics: A new approach to modeling multi-dimensional detonation waves. In *Ninth Symposium (Int.) on Detonation*, pages 730–742, Portland, OR, 1989. Office of Naval Research, OCNR 113291-7.

[8.] D. S. Stewart and J. B. Bdzil. *Combustion and Flame*, 72:311, 1988.

[9.] T. D. Aslam J. B. Bdzil and D. S. Stewart. Curved detonation fronts in solid explosives: collisions and boundary interactions. In *Proceedings of the 20th International Symposium on Shock Waves*, pages 97–106, Pasadena, CA, 1995. International Symposia on Shock Waves, World Scientific Publishing.

[10.] R. P. Fedkiw, T. D. Aslam, B. Merriman, and S. Osher. A non-oscillatory eulerian approach to interfaces in multimaterial flows (the ghost fluid method). *J. Comput. Phys.*, 1999. accepted.

[11.] J. J. Quirk. *Intl J. Numer. Meth. Fluids*, 18:555, 1994.

[12.] C. Shu and S. Osher. *J. Comput. Phys.*, 77:439, 1988.

[13.] X. D. Liu and S. Osher. *J. Comput. Phys.*, 142:304, 1998.

[14.] R. R. Critchfield, B. W Asay, J. B. Bdzil, W. C. Davis, E. N. Ferm, and D. J. Idar. Synchro-ballistic recording of detonation phenomena. *Proc. SPIE*, 3173:99, 1997.